Volume 2
Number 23
7 December 2021
Pages 7493–7790

Materials Advances

rsc.li/materials-advances

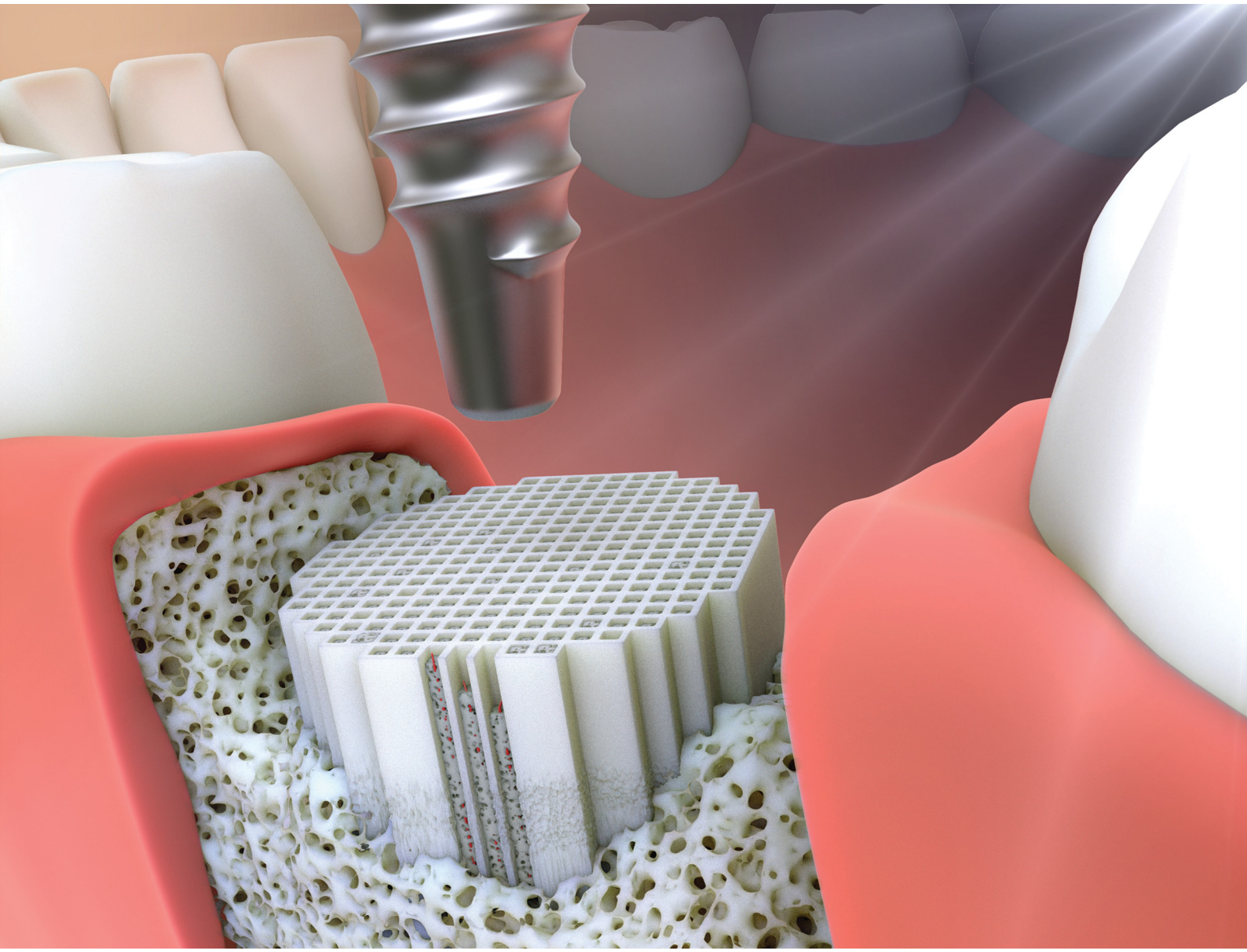

ISSN 2633-5409

ROYAL SOCIETY OF CHEMISTRY

PAPER
Koichiro Hayashi *et al.*
Honeycomb scaffolds capable of achieving barrier membrane-free guided bone regeneration

Materials Advances

ROYAL SOCIETY OF CHEMISTRY

PAPER

View Article Online
View Journal | View Issue

Check for updates

Cite this: *Mater. Adv.*, 2021, 2, 7638

Honeycomb scaffolds capable of achieving barrier membrane-free guided bone regeneration

Koichiro Hayashi, * Masaya Shimabukuro, Ryo Kishida, Akira Tsuchiya and Kunio Ishikawa

Barrier membrane-free guided bone regeneration (GBR) with a synthetic scaffold may resolve the current challenges in vertical bone augmentation. To realize such GBR, we fabricated carbonate apatite honeycomb (HC) scaffolds capable of preventing soft tissue invasion and enhancing bone ingrowth. These HC scaffolds with 230-, 460-, and 630 μm-aperture channels were designated as HC230, HC460, and HC630, respectively. They were constructed by interconnecting carbonate apatite microspheres; they possessed micropores and nanopores in the struts and were implanted on the rabbit calvarium. The amount of new bone and soft tissues in the HC scaffolds significantly increased and decreased, respectively, with the decrease in the channel aperture size. The new bone height in HC230 at 4 and 12 weeks post-implantation was 3.4 ± 0.5 and 3.8 ± 0.2 mm, respectively, reaching the top edge of the struts. The percent volume of new bone in HC230 at 4 and 12 weeks post-implantation was 38.6% ± 2.2% and 49.9% ± 1.5%, respectively. These findings demonstrated that HC230 augmented faster, higher, and a greater amount of vertical bone growth than the reported combinations of scaffolds and growth factors or barrier membranes. Therefore, the multiscale-architectural control of HC scaffolds may pioneer barrier membrane-free GBR.

Received 6th August 2021,
Accepted 28th September 2021

DOI: 10.1039/d1ma00698c

rsc.li/materials-advances

Open Access Article. Published on 28 September 2021. Downloaded on 10/6/2024 4:17:07 PM.
This article is licensed under a Creative Commons Attribution 3.0 Unported Licence.

Introduction

Long-term clinical success of dental implants depends on the height and volume of the alveolar bone available.[1,2] Therefore, alveolar bone augmentation is necessary when there is insufficient bone. Among various bone loss configurations, the augmentation of bone loss vertically is extremely challenging owing to the low supply of osteogenic cells from the residual bone.[3,4]

The gold standard for vertical bone augmentation is autogenous bone graft. However, autogenous bone grafts have several limitations, such as (1) donor site morbidity, which reaches 25%; (2) post-surgery pain; (3) nerve and soft-tissue injuries; (4) increased intra-operative time; (5) limitation in the quantity of bone harvested; and (6) reduced amount of harvested bone, because the majority of the osteogenic cells in the harvested graft do not survive the harvest and transplantation procedures.[5–9]

Guided bone regeneration (GBR) is another common technique for bone augmentation.[10–12] The advantage of GBR is that it hinders the unwanted migration of faster-growing epithelial cells and connective tissue fibroblasts into the bone defect, thereby allowing the migration of slower-growing osteogenic cells.[10–12] To achieve this principle in GBR, a barrier membrane that physically blocks the invasion of soft tissues into the bone defect is placed between the soft tissues and bone defect.[10–12] Bone grafts and substitute materials are implanted in the bone defect to provide structural support and promote bone regeneration.

GBR provides a relatively predictable outcome for bony defects.[13] Nevertheless, GBR still provides limited and unpredictable bone for vertical extra-cortical bone augmentation, and the frequency of complications and failures is too high (well over 20%).[14–16] These unfavorable outcomes of GBR for vertical bone augmentation could be attributed to the use of barrier membranes. Currently used barrier membranes are divided into non-resorbable and resorbable.[17] The use of non-resorbable barrier membranes (*e.g.*, polytetrafluoroethylene, expanded polytetrafluoroethylene membrane, and titanium mesh) requires a secondary surgery for membrane removal, and the membrane stiffness often causes soft tissue dehiscence, resulting in wound infection and an extended healing period.[18–22] Resorbable barrier membranes (*e.g.*, polylactide, polyglycolide, polycaprolactone, and collagen) provide less volume stability during bone repair, because of the faster resorption, than the complete bone regeneration (3–6 months), resulting in the premature loss of mechanical properties.[23] The biodegradation of these membranes causes an inflammatory reaction in the soft tissue.[24] Considering these

Department of Biomaterials, Faculty of Dental Science, Kyushu University, 3-1-1 Maidashi, Higashi-ku, Fukuoka 812-8582, Japan.
E-mail: khayashi@dent.kyushu-u.ac.jp

© 2021 The Author(s). Published by the Royal Society of Chemistry

Open Access Article. Published on 28 September 2021. Downloaded on 10/6/2024 4:17:07 PM.
This article is licensed under a Creative Commons Attribution 3.0 Unported Licence.

severe problems associated with autologous bone and barrier membranes, GBR with only synthetic scaffolds without a barrier membrane, which we named "barrier membrane-free GBR," would be ideal for bone augmentation.

Granular scaffolds are widely used as bone substitute materials for intra-bone defects in the dental field. For vertical bone augmentation, block-type scaffolds are considered favorable, because they facilitate shape forming and maintain the handleability, which are difficult when granular scaffolds are used. Various block-type scaffolds have been reported;[25,26] however, their ability for vertical bone augmentation is limited, and they need a combination of bone morphogenetic protein (BMP),[26–28] growth factors,[29] and stem and/or progenitor cells for favorable outcomes.[30–34] These combination approaches have several limitations, including severe swelling, cyst-like tissue formation, high cost, osteoclastic bone resorption, cumbersome procedures, and/or invasive manipulation requiring a minimum of two surgeries.[35–37]

Scaffolds with uniaxial channels from the bottom face contacting the host bone to the top face, such as honeycomb (HC) scaffolds, are favorable for vertical bone augmentation, compared to three-dimensional (3D) porous scaffolds.[38] In 3D porous scaffolds, pores are present in all peripheries. Therefore, a large portion of the 3D porous scaffold is in contact with fibrous tissues, facilitating the entrance of fibrous tissues into the scaffold. In contrast, uniaxial channels in HC scaffolds open only in the specific two faces, thereby restricting the entry of fibrous tissues. In HC scaffolds, one edge of the channel contacts the host bone and the fibrous tissues enter only from the other edge of the channel. Therefore, by promoting fast bone ingrowth from the HC scaffold face contacting the host bone, compared to the fibrous tissue ingrowth from the other face, barrier membrane-free GBR could be achieved.

The pore size of the barrier membrane in the GBR influences the invagination of soft tissue and the penetration of oxygen, nourishment, and fluid required for osteogenesis.[10–12,39] The channels of the HC scaffolds can be considered as pores of the barrier membrane. Previously, we demonstrated that osteogenesis in the HC scaffolds could be controlled by controlling their channel size.[40,41] We did not evaluate the effects of channel aperture size $>$ 300 μm on the tissue responses; however, we demonstrated that both osteogenesis and angiogenesis were substantially promoted when the channel aperture size was $>$ 230 μm.[40,41] Based on these findings, we hypothesize that controlling the HC channel aperture size could make the bone ingrowth dominant, compared to that of the soft tissue ingrowth.

In addition, we demonstrated that the osteoconductivity and bioresorbability of HC scaffolds could be controlled by controlling their micropore and nanopore structures.[42,43] The chemical composition of HC scaffolds affects their osteoconductivity and bioresorbability. HC scaffolds composed of carbonate apatite (CAp), that is, bone mineral, are superior in terms of replacement by new bone, than β-tricalcium phosphate (TCP) and hydroxyapatite (HAp).[44,45] Based on these findings, we fabricated HC scaffolds by interconnecting CAp microspheres (~5 μm in diameter), to introduce micropores and nanopores to HC struts, resulting in enhanced osteogenesis and angiogenesis.[41]

In this study, we fabricated three types of HC scaffolds by interconnecting CAp microspheres with different channel aperture sizes (~230, 460, and 630 μm). We demonstrated the effects of HC channel aperture size on the ingrowth of bone and soft tissues by evaluating vertical bone augmentation of these HC scaffolds on the rabbit calvarium.

Results

Fabrication and characterization of HC scaffolds

A mixture of $CaCO_3$ microspheres (~5 μm in diameter) and methylcellulose-based binder was extruded through a die with a slit thickness of 200 μm and pitch of 500, 700, or 900 μm (Fig. 1a). The obtained HC green bodies were heated at 600 °C for 24 h to remove the binder (Fig. 1b), resulting in the formation of $CaCO_3$ HC blocks. The $CaCO_3$ HC blocks were immersed in 1 mol L^{-1} Na_2HPO_4 solution at 80 °C for 7 days (Fig. 1c). The CAp HC scaffolds were formed *via* dissolution–precipitation reaction; they were precisely shaped into cylinders (diameter = 6 mm, height = 4 mm) using computer-aided design and computer-aided manufacturing (Fig. 1d). The shaped HC scaffolds were implanted on the rabbit calvarium to evaluate their ability of vertical bone augmentation and the effects of channel size on the ingrowth of bone and soft tissues (Fig. 1e).

Cylindrical HC scaffolds were comprised of uniaxially penetrating channels, and the channel edges opened on both the bases of the cylinder (Fig. 2a–f). The channel aperture size, that is, edge-to-edge length of a square channel aperture, was 231 ± 11 (Fig. 2g), 461 ± 6 (Fig. 2h), and 631 ± 5 μm (Fig. 2i); henceforth, these HC scaffolds are designated as HC230, HC460, and HC630, respectively. The strut thickness of HC230, HC460, and HC630 was 179 ± 5 (Fig. 2g), 180 ± 3 (Fig. 2h), and 183 ± 4 μm (Fig. 2i), respectively. All three HC scaffolds had almost equal-sized struts, and the struts were constructed by interconnecting microspheres that scaly crystals characteristic of apatite aggregated into (Fig. 2j–l). There was a space of $<$2 μm between the adjoining microspheres in the struts (Fig. 2j–l), and they served as micropores/nanopores.

The X-ray diffraction (XRD) patterns of HC230, HC460, and HC630 were consistent with that of commercial CAp (Fig. 3a). This implies that the chemical composition of these scaffolds transformed from $CaCO_3$ to CAp *via* a dissolution–precipitation reaction maintained the HC architecture. The Fourier transform infrared (FT-IR) spectra of HC230, HC460, and HC630 exhibited the absorption bands because of the phosphate (1140–975 and 615–515 cm^{-1}) in the apatite crystal (Fig. 3b). Doublet bands corresponding to carbonate in A-(1480 cm^{-1}) and B-type (1415 cm^{-1}) CAp[46,47] were present in the spectra of HC230, HC460, and HC630. In the HAp spectrum, the carbonate bands were absent and a hydroxyl band was present at 626 cm^{-1}. These results demonstrate that HC230, HC460, and

Open Access Article. Published on 28 September 2021. Downloaded on 10/6/2024 4:17:07 PM.
This article is licensed under a Creative Commons Attribution 3.0 Unported Licence.

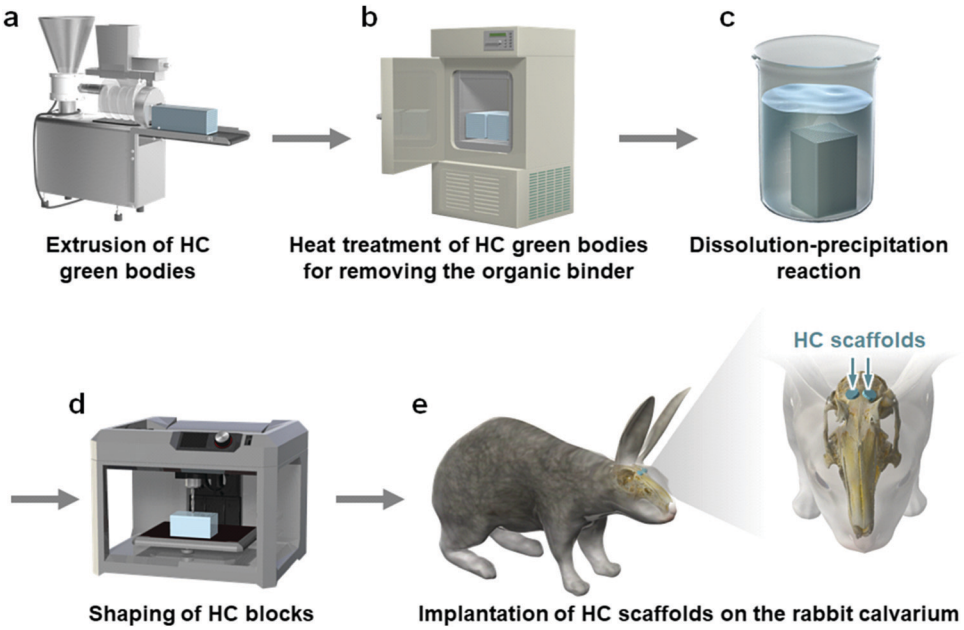

Fig. 1 Schematic illustration of the fabrication procedure of CAp HC scaffolds and animal experiments. (a) Extrusion of HC green bodies. (b) Heat treatment of HC green bodies for removing the organic binder, resulting in the formation of $CaCO_3$ HC blocks. (c) Dissolution–precipitation reaction of $CaCO_3$ HC blocks, converting the chemical composition from $CaCO_3$ to CAp. (d) Precise shaping of CAp HC blocks into cylinders of 6 mm in diameter and 4 mm in height by computer-aided design and computer-aided manufacturing. (e) The implantation of cylindrical HC scaffolds on the rabbit calvarium.

HC630 were AB-type CAp, in which both the hydroxyl and phosphate are replaced by carbonate.[47] Elemental analyses revealed that the carbonate content in HC230, HC460, and HC630 was 6%–10%, which was similar to the carbon content in human bones.[48]

The porosity of HC230, HC460, and HC630 was 65.9% ± 1.6%, 77.5% ± 0.7%, and 82.1% ± 0.8%, respectively (Fig. 4a). The porosity increased with increasing channel aperture size. The compressive strength of HC230, HC460, and HC630 was 27.5 ± 3.6, 17.3 ± 2.6, and 12.3 ± 3.4 MPa, respectively (Fig. 4b). The compressive strength decreased with increasing porosity or channel aperture size.

Animal Experiments

The micro-computed tomography (μ-CT) images showed that HC230, HC460, and HC630 retained their original shape, that is, outline and HC structure, at 4 weeks post-implantation (Fig. 5a–c). The interior of the channels in HC230 appeared whitish (Fig. 5a). In contrast, black regions remained within the channels of HC460 (Fig. 5b) and HC630 (Fig. 5c). The HC630 channels contained more extensive black regions than the HC230 channels. Whitish and black regions were presumed to be the regions dominated by newly formed bone and soft tissues, respectively. Therefore, the above results suggested that new bone had already formed in the HC230 channels at 4 weeks post-implantation, whereas soft tissues were dominant in the channels of HC460 and HC630. At 12 weeks post-implantation, in all HC scaffolds, the new bone region within their channels was extended, compared with that at 4 weeks (Fig. 5d–f). The lower region of HC230 was replaced by new bone (Fig. 5d). In all HC scaffolds, a portion of the struts was resorbed (Fig. 5d–f). The top surfaces of these HC scaffolds are rounded due to the pressure from fascia covering their top surfaces (Fig. 5d–f). This tendency was considerable in HC630; HC630 had less tolerance to pressure than HC230 and HC460. This could be attributed to the fewer number of struts, which indicates lower mechanical strength in HC630 than in HC230 and HC460. The percent volume of the remaining materials (Fig. 5g) and newly formed bone (Fig. 5H) were estimated based on the μ-CT images. The percent volume of the remaining materials was as follows: 56.2% ± 3.3%, 41.3% ± 2.2%, and 31.8% ± 4.2% at 4 weeks post-implantation and 37.5% ± 10.4%, 24.5% ± 3.7%, and 17.2% ± 1.2% at 12 weeks post-implantation for HC230, HC460, and HC630, respectively (Fig. 5g). The percent volume of new bone was as follows: 38.6% ± 2.2%, 29.8% ± 5.0%, and 24.3% ± 2.5% at 4 weeks post-implantation and 49.9% ± 1.5%, 37.1% ± 3.4%, and 32.3% ± 5.1% at 12 weeks post-implantation for HC230, HC460, and HC630, respectively (Fig. 5h). The percent volume of the remaining materials and new bone significantly decreased and increased, respectively, in all groups between weeks 4 and 12 post-implantation. The percent volume of the remaining materials and new bone increased significantly with the increase in the channel aperture size. In HC230, the total percent volume of the remaining materials and new bone at 4 and 12 weeks post-implantation was ~95% and ~87%, respectively. These values were significantly higher than those in HC460 and HC630, which were ~71% and ~60% at 4 weeks post-implantation, and ~62% and ~50% at 12 weeks post-implantation, respectively. These results indicate that HC230 elicited preferential ingrowth of

© 2021 The Author(s). Published by the Royal Society of Chemistry

Open Access Article. Published on 28 September 2021. Downloaded on 10/6/2024 4:17:07 PM.
This article is licensed under a Creative Commons Attribution 3.0 Unported Licence.

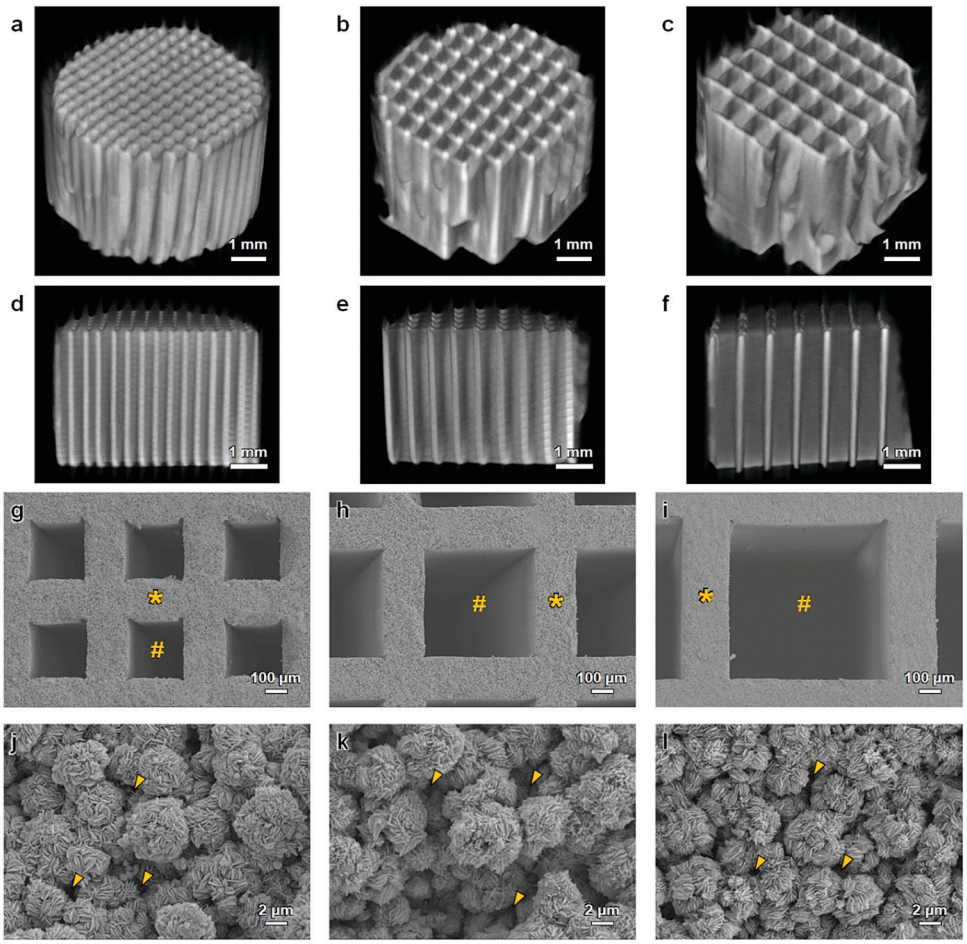

Fig. 2 μ-CT images of (a) HC230, (b) HC460, and (c) HC630. Longitudinal sections of (d) HC230, (e) HC460, and (f) HC630. SEM images of (g) HC230, (h) HC460, and (i) HC630: "*" and "#" indicate strut and channel, respectively. Magnified views of the struts in (j) HC230, (k) HC460, and (l) HC630: arrow heads indicate micropores and nanopores.

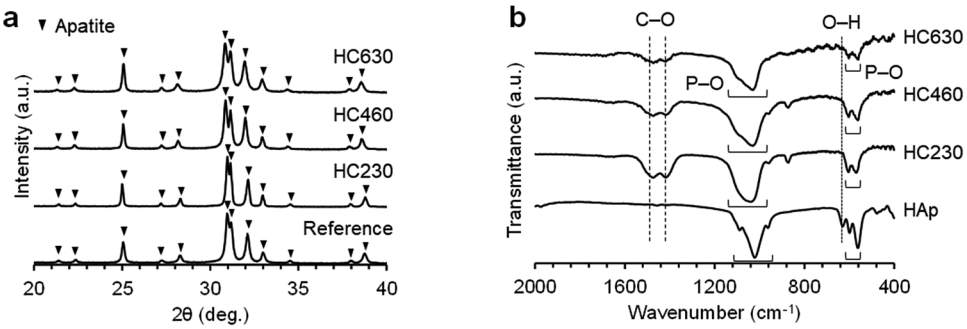

Fig. 3 (a) XRD patterns of HC230, HC460, and HC630. Commercial CAp granules were used as a reference. (b) FT-IR spectra of HC230, HC460, and HC630. HAp was used as a reference.

bone in the early stage, whereas HC460 and HC630 caused the ingrowth of other tissues, such as soft tissues, rather than bone. Thereafter, HC230 was steadily replaced by new bone, including blood vessels, whereas HC460 and HC630 were replaced by both bone and soft tissues.

The tissues formed within the HC scaffolds were histologically analyzed. At 4 weeks post-implantation in HC230 (Fig. 6a), new bone was formed along the struts (Fig. 6A1–A3) and blood vessels were present in the center of the channel, whereas bone continued to form on the struts (Fig. 6A1–A6). The new bone reached the top edge of the struts, that is, the top surface of the scaffold, at 4 weeks post-implantation (Fig. 6A1 and A4). Osteoblasts added new material on the surface of new bone and osteoclasts resided on the struts (Fig. 6A4–A6).

Open Access Article. Published on 28 September 2021. Downloaded on 10/6/2024 4:17:07 PM.
This article is licensed under a Creative Commons Attribution 3.0 Unported Licence.

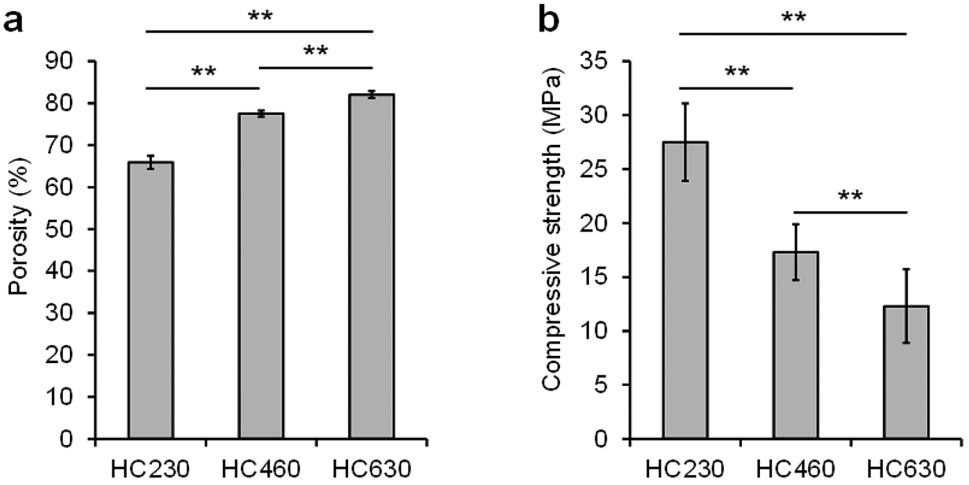

Fig. 4 (a) Porosities and (b) compressive strengths of HC230, HC460, and HC630.

In HC460 (Fig. 6b), fibrous tissues occupied the upper region of the channels (Fig. 6B1 and B4) and new bone formed in the middle (Fig. 6B2 and B5) and the lower (Fig. 6B3 and B6) regions. However, fibrous tissues were dominant in the middle region (Fig. 6B2 and B5), and a small amount of fibrous tissue reached the bottom region (Fig. 6B3 and B6). Osteoblasts and osteoclasts were present on the new bone and struts, respectively (Fig. 6B5 and B6). In HC630 (Fig. 6c), the channels in the upper (Fig. 6C1 and C4) and middle (Fig. 6C2 and C5) regions were dominated by fibrous tissues. In the bottom region, fibrous tissues were extensively present; however, there was new bone formation (Fig. 6C4 and C6). Osteoblasts and osteoclasts resided on the new bone and the struts, respectively (Fig. 6C5 and C6).

At 12 weeks post-implantation, a new bone formed extensively in the entire inner side of the channels from the bottom

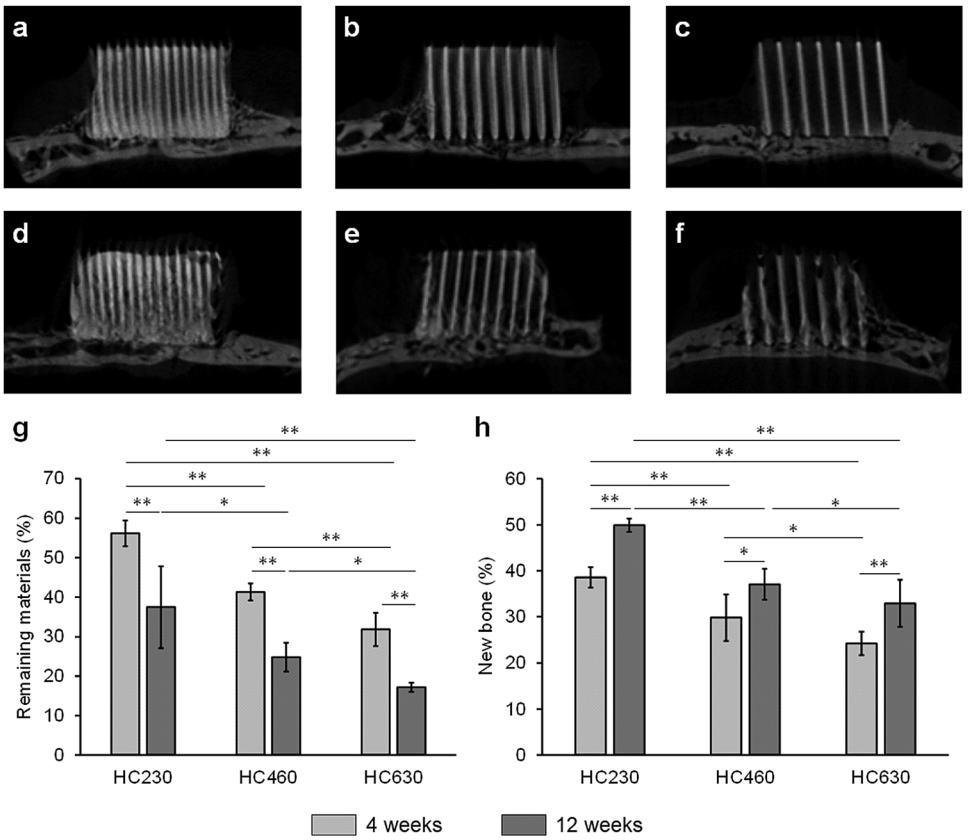

Fig. 5 μ-CT images of (a) HC230, (b) HC460, and (c) HC630 at 4 weeks post-implantation; (d) HC230, (e) HC460, and (f) HC630 at 12 weeks post-implantation. The percent volumes of the (g) remaining materials and (h) new bone at 4 and 12 weeks post-implantation. *$p < 0.05$ and **$p < 0.01$.

© 2021 The Author(s). Published by the Royal Society of Chemistry

Open Access Article. Published on 28 September 2021. Downloaded on 10/6/2024 4:17:07 PM.
This article is licensed under a Creative Commons Attribution 3.0 Unported Licence.

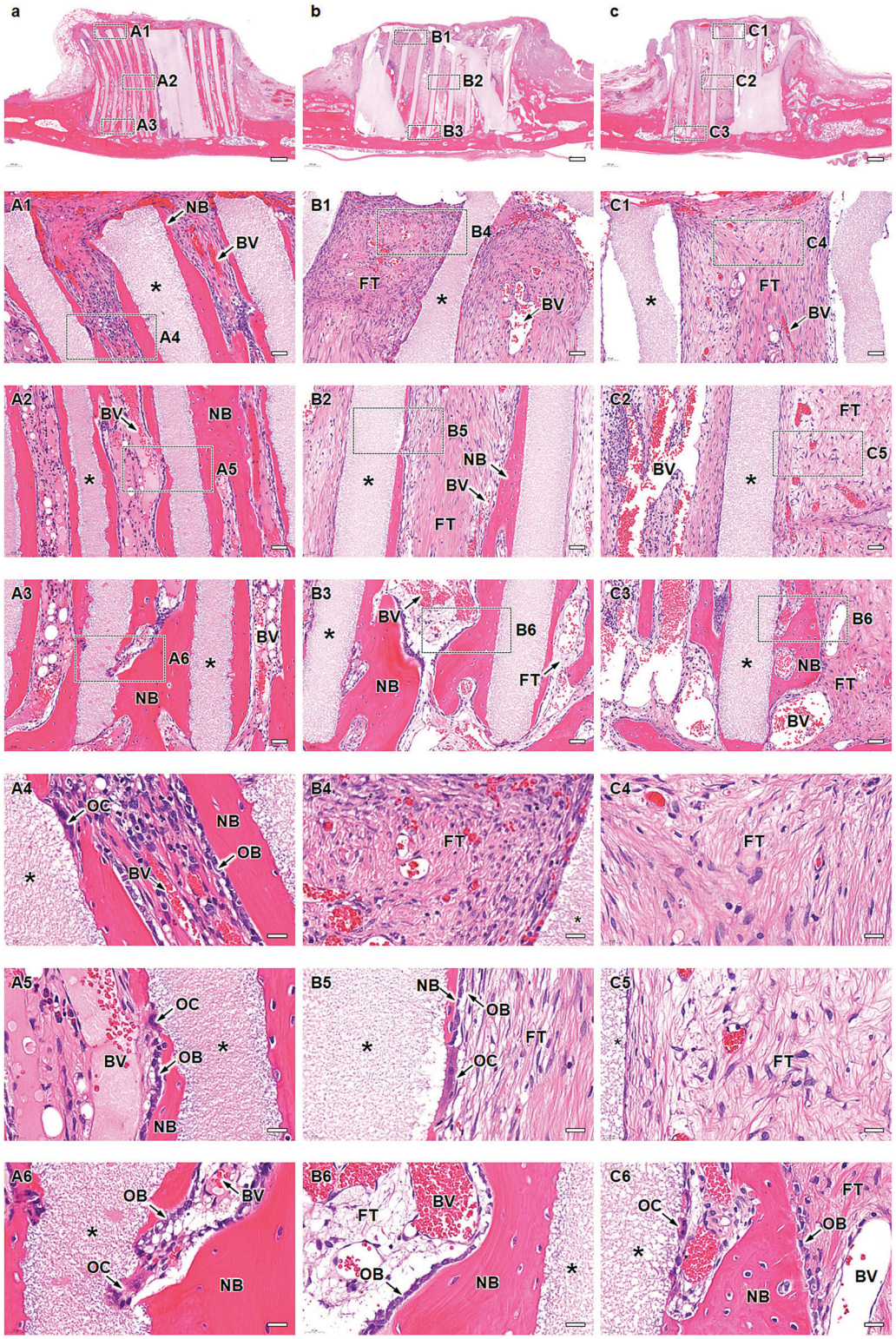

Fig. 6 Histological micrographs at 4 weeks post-implantation of (a) HC230, (b) HC460, and (c) HC630. (a–c) Overviews; scale bar = 500 μm. (A1–A3) Magnified images of the regions (A1–A3) shown in image a; scale bar = 50 μm. (A4–A6) Higher magnified images of the regions (A4–A6) shown in images (A1–A3); scale bar = 20 μm. (B1–B3) Magnified images of the regions (B1–B3) shown in image b; scale bar = 50 μm. (B4–B6) Higher magnified images of the regions (B4–B6) shown in images (B1–B3); scale bar = 20 μm. (C1–C3) Magnified images of the regions (C1–C3) shown in image c; scale bar = 50 μm. (C4–C6) Higher magnified images of the regions (C4–C6) shown in images (C1–C3); scale bar = 20 μm. "*," "NB," "BV," "FT," "OB," and "OC" indicate strut, new bone, blood vessel, fibrous tissue, osteoblast, and osteoclast, respectively.

Open Access Article. Published on 28 September 2021. Downloaded on 10/6/2024 4:17:07 PM.
This article is licensed under a Creative Commons Attribution 3.0 Unported Licence.

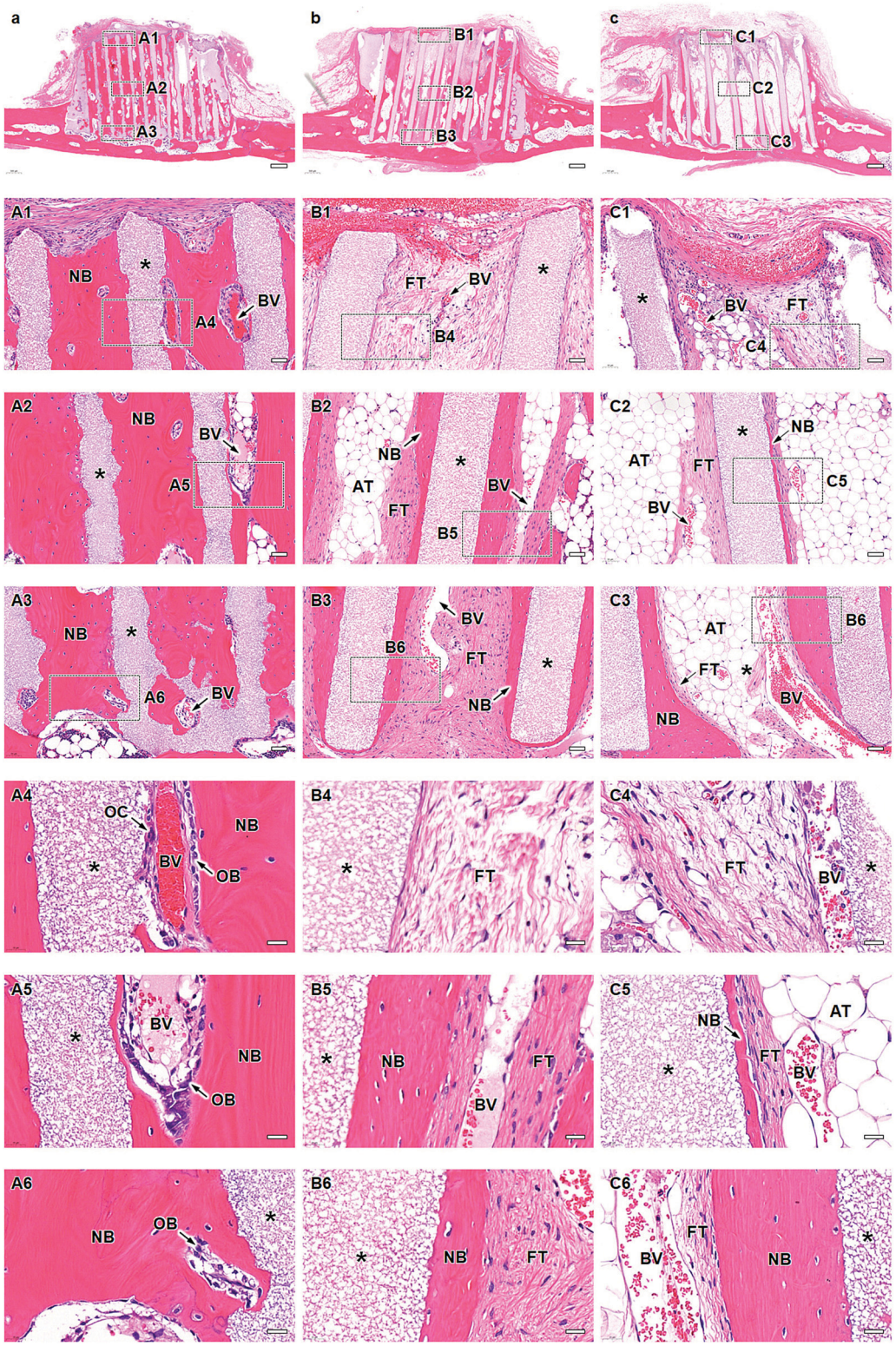

Fig. 7 Histological micrographs at 12 weeks post-implantation of (a) HC230, (b) HC460, and (c) HC630. (a–c) Overviews; scale bar = 500 μm. (A1–A3) Magnified images of the regions (A1–A3) shown in image a; scale bar = 50 μm. (A4–A6) Higher magnified images of the regions (A4–A6) shown in images (A1–A3); scale bar = 20 μm. (B1–B3) Magnified images of the regions (B1–B3) shown in image b; scale bar = 50 μm. (B4–B6) Higher magnified images of the regions (B4–B6) shown in images (B1–B3); scale bar = 20 μm. (C1–C3) Magnified images of the regions (C1–C3) shown in image c; scale bar = 50 μm. (C4–C6) Higher magnified images of the regions (C4–C6) shown in images (C1–C3); scale bar = 20 μm. "*," "NB," "BV," "FT," "OB," "OC," and "AT" indicate strut, new bone, blood vessel, fibrous tissue, osteoblast, osteoclast, and adipose tissue, respectively.

© 2021 The Author(s). Published by the Royal Society of Chemistry

Open Access Article. Published on 28 September 2021. Downloaded on 10/6/2024 4:17:07 PM.
This article is licensed under a Creative Commons Attribution 3.0 Unported Licence.

to the top in HC230 (Fig. 7A1–A3). The new bone included blood vessels (Fig. 7A1–A6), and several osteoblasts were present on the new bone (Fig. 7A4–A6). Osteoclasts resided on the struts (Fig. 7A4); however, the number decreased from that at 4 weeks post-implantation. In HC460 (Fig. 7b), fibrous tissues dominated the upper region (Fig. 7B1 and B4). In the middle (Fig. 7B2 and B5) and lower (Fig. 7B3 and B6) regions, fibrous tissues remained; however, the amount of new bone increased from that at 4 weeks post-implantation. In HC630 (Fig. 7C), fibrous tissues still occupied the channels in the upper regions (Fig. 7C1 and C4). In the middle region, a small amount of new bone formed on a portion of the struts; however, fibrous tissues occupied a large portion of the struts, and they were present on the new bone (Fig. 7C2 and C5). Adipose tissues dominated the interior of the channels except for the strut surface (Fig. 7C2 and C5). In the lower region (Fig. 7C3 and C6), new bone formed on the struts and fibrous tissues resided on the new bone, whereas adipose tissues filled the channel center (Fig. 7C3 and C6). The main components of soft tissues were fibrous tissues at 4 weeks post-implantation; however, adipose tissues replaced fibrous tissues at 12 weeks post-implantation. This behavior was most pronounced in HC630, followed by that in HC460, but it was only slightly observed in HC230. Adipose tissues appeared to migrate from bone marrow in the host bone. These results suggested that the migration speed and the passable size of soft tissues varied with their type. The channel size influenced the formation of both bone and soft tissues in the HC scaffolds.

The height and percent area of new bone and the percent area of fibrous tissues in each channel were estimated from hematoxylin-eosin (HE)-stained sections. The height of the newly formed bone in each channel was as follows (Fig. 8a): 3.4 ± 0.5, 1.6 ± 1.3, and 1.2 ± 1.0 mm at 4 weeks post-implantation and 3.8 ± 0.2 mm, 3.0 ± 0.5 mm, and 2.5 ± 0.7 mm at 12 weeks post-implantation for HC230, HC460, and HC630, respectively. HC230 promoted substantial bone ingrowth and induced new bone, ~2- and ~3-fold higher than that by HC460 and HC630, respectively, at 4 weeks post-implantation. At 12 weeks post-implantation, HC230 maintained a bone height significantly higher than that in HC460 and HC630. The percent area of new bone in each channel was as follows (Fig. 8b): 29.2% ± 7.9%, 13.5% ± 7.9%, and 7.5% ± 4.2% at 4 weeks post-implantation and 42.4% ± 8.6%, 26.8% ± 7.1%, and 14.0% ± 4.7% at 12 weeks post-implantation for HC230, HC460, and HC630, respectively. The percent area of new bone in HC230 was ~2 and ~4 times larger than that in HC460 and HC630, respectively, at 4 weeks post-implantation. At 12 weeks post-implantation, HC230 maintained a larger percent area of new bone than that by HC460 and HC630. The percent area of fibrous tissues in each channel was as follows (Fig. 8c): 19.4% ± 5.4%, 47.1% ± 10.5%, and 60.0% ± 9.3% at 4 weeks post-implantation and 5.7% ± 2.5%, 13.8% ± 6.2%, and 30.1% ± 10.7% at 12 weeks post-implantation for HC230, HC460, and HC630, respectively. HC230 suppressed the invasion of fibrous tissue below 40% and 30% of that in HC460 and HC630, respectively.

Discussion

This study demonstrated that controlling the channel aperture size of HC scaffolds is effective in enhancing bone ingrowth and preventing the invasion of soft tissues, such as fibrous and adipose tissues. For bone ingrowth, the 230 μm channel resulted in the highest osteogenesis, and osteogenesis decreased with increasing channel aperture size. Furthermore, in our previous studies, we evaluated the effects of channel aperture size in the 100 to 300 μm range and demonstrated that osteogenesis and angiogenesis were significantly promoted when the channel aperture size was >230 μm.[40,41] These findings

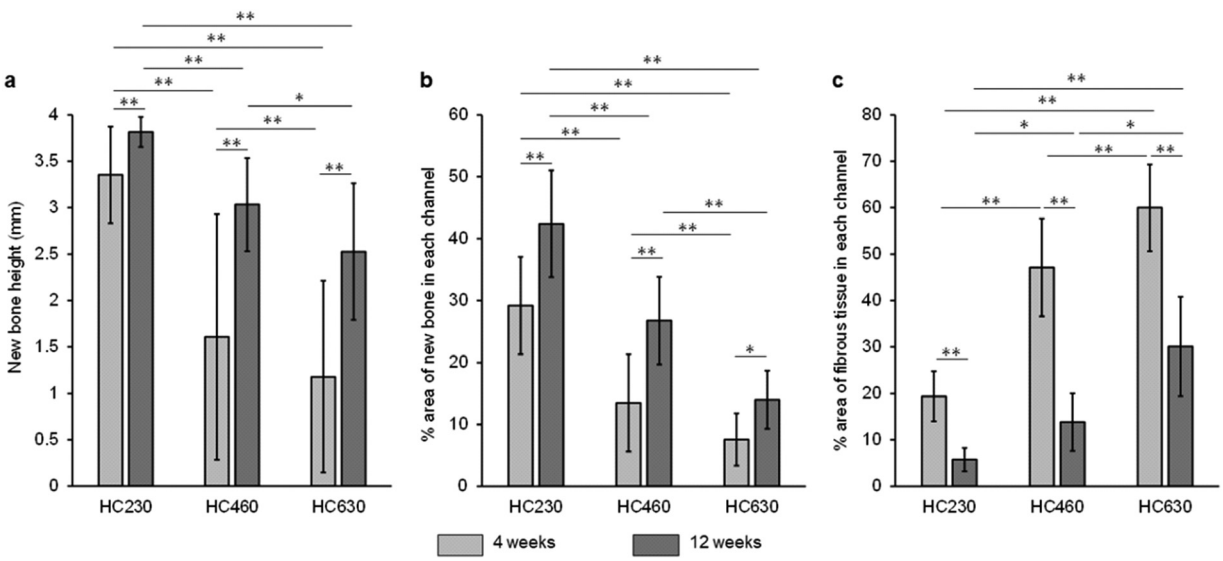

Fig. 8 (a) New bone height, (b) percentage area of new bone in each channel, (c) percentage area of fibrosis tissues in each channel at 4 and 12 weeks post-implantation of HC230, HC460, and HC630. *$p < 0.05$ and **$p < 0.01$.

Open Access Article. Published on 28 September 2021. Downloaded on 10/6/2024 4:17:07 PM.
This article is licensed under a Creative Commons Attribution 3.0 Unported Licence.

indicate that the optimum channel aperture size for osteogenesis is ~230 μm in the 100 to 630 μm range.

With respect to the invasion of fibrous tissues into the HC scaffolds, the ability to suppress this invasion increased with decreasing channel aperture size. Channels with an aperture size of 230 μm substantially suppressed the invasion of fibrous tissues into the HC scaffolds, compared to channels with aperture sizes of 460 and 630 μm. Guo *et al.* reported that the use of zinc barrier membrane with 300 μm pores confined fibrous tissues to the outer surface of the membrane, whereas the use of zinc barrier membrane with 1000 μm pores allowed the entry of fibrous tissues *via* the pores.[49] The findings by Guo *et al.* are consistent with the findings of this study. Therefore, ~230 μm is an appropriate channel aperture size to achieve both dominant bone ingrowth and the inhibition of fibrous tissue invasion. The fibrous tissues formed in the channels were gradually replaced by adipose tissues. Lee *et al.* reported that fibrous tissues decreased approximately by half from weeks 2 to 8 post-implantation, and alternatively, adipose tissues appeared at 8 weeks post-implantation.[50] The findings reported by Lee *et al.* are consistent with our findings in this study. Channel aperture size is a key factor regulating the ingrowth of bone and soft tissues, including fibrous tissues and adipose tissues.

The HC scaffolds with 230 μm-aperture size channels achieved both favorable bone ingrowth and inhibition of fibrous tissue invasion. Bone ingrowth and the invasion of fibrous tissues compete for the interior channel space in the HC scaffolds. In general, higher osteoconductivity facilitates the domination of new bone in the channel space. Osteoconductivity is influenced by the chemical composition, channel aperture size, and microporous and nanoporous structures. These properties of the HC scaffolds are optimized based on the findings of our previous studies,[40–43] resulting in high osteoconductivity. Furthermore, in this study, the histological results demonstrated that new bone formed on the struts of HC scaffolds and blood vessels formed in the center of the HC scaffold channels, which indicates that osteogenic cells resided on the struts before the formation of blood vessels within the channels. Additionally, the occupancy of osteogenic cells on the strut resulted in decreased open channel space, making the invasion of fibrous tissues into the HC scaffolds more difficult. On the contrary, blood vessels are key to differentiating osteogenic cells, forming new bone, and maintaining bone. Therefore, the channel aperture size after the occupancy of osteogenic cells on the strut surface should be controlled to be within the size range that allows the penetration of blood vessels. Blood vessels can enter 40 μm pores, whereas fibrous tissues require >75 μm pores for long-term ingrowth.[51] Artificial skin and meshes for hernia repair have 100 and 75 μm pores, respectively.[52,53] Therefore, when the channel aperture size is 40–100 μm after the occupancy of osteogenic cells, osteoblasts, and/or bone on the struts, the formation of blood vessels is deemed to become dominant over the fibrous tissue ingrowth. In this study, the histological results demonstrated that the channel aperture size was 40–100 μm after bone formation on the struts of HC230. Therefore, the 230 μm-aperture size channels successfully allowed the formation of blood vessels and suppressed the invasion of fibrous tissues.

The height of the bone newly formed in HC230 at 4 and 12 weeks post-implantation was 3.4 ± 0.5 and 3.8 ± 0.2 mm, respectively. These reached the limiting values in the vertical bone augmentation model on the rabbit calvarium, because the scaffold height should be <4 mm for complete closure of the scaffolds by suturing the fasciae. The percent volume of new bone in HC230 at 4 and 12 weeks post-implantation was 38.6% ± 2.2% and 49.9% ± 1.5%, respectively. We assessed the capacity of HC230 for vertical bone augmentation *via* comparison with the findings of previous studies in terms of height and volume of new bone, evaluated using the vertical bone augmentation model on the rabbit calvarium. Kim *et al.* reported that when calcium sulfate granule-filled rings were implanted, the new bone height at 2 and 8 weeks post-implantation was 1.2 ± 0.7 and 2.6 ± 1.1 mm, respectively.[54] When combined with calcium sulfate and molecules such as sodium butyrate and dimethyloxalylglycine that promote bone regeneration, the new bone height at 2 and 8 weeks post-implantation was 1.0 ± 0.3 and 3.2 ± 0.5 mm, respectively.[54] The maximum height of the newly formed bone in brushite, combined brushite and anabolic conjugate drug, monetite, and combined monetite and anabolic conjugate drug at 12 weeks post-implantation was 0.8 ± 0.2, 1.7 ± 0.6, 1.4 ± 0.4, and 2.7 ± 0.5 mm, respectively.[55] The percent volume of the newly formed bone in combined recombinant human vascular endothelial growth factor (rhVEGF) and HAp blocks at 4 and 6 weeks post-implantation was 0.8% ± 0.6% and 0.8% ± 0.5%, respectively.[56] The percent volume of new bone at 14 weeks post-implantation of recombinant human BMP 2 (rhBMP-2)-containing collagen sponges in conjunction with β-TCP, biphasic calcium phosphate, bovine bone mineral, and blood clot was 28.7% ± 4.6%, 31.9% ± 5.1%, 18.0% ± 2.2%, and 15.3% ± 2.9%, respectively.[57] The percent volume of new bone formed in 3D printed porous TCP/HAp block-, anorganic bovine bone-, or TCP-filled titanium hemispheres was 23% ± 1.6%, 13.6% ± 1.5%, and 13.8% ± 1.5% at 8 weeks post-implantation and 35% ± 2%, 39% ± 2%, and 43% ± 6% at 16 weeks post-implantation, respectively.[58] Therefore, using only HC230 augments faster, higher, and more vertical bone growth than using the various combinations of scaffolds and supplements promoting bone formation (BMP, VEGF, sodium butyrate, dimethyloxalylglycine, and anabolic conjugate drug) or barriers for soft tissue invasion, such as titanium hemisphere. The excellent ability of HC230 for vertical bone augmentation is probably due to its controlled pore architecture (channels, micropores, and nanopores) and chemical composition. Therefore, HC scaffolds have a tremendous potential for realizing barrier membrane-free GBR. A limitation of this study is that the evaluation periods were shorter than those required for complete replacement of the HC scaffolds by new bone. In a future study, long-term evaluation of vertical bone augmentation using HC scaffolds is required.

© 2021 The Author(s). Published by the Royal Society of Chemistry

Open Access Article. Published on 28 September 2021. Downloaded on 10/6/2024 4:17:07 PM.
This article is licensed under a Creative Commons Attribution 3.0 Unported Licence.

Experimental

Fabrication of HC scaffolds

A mixture of $CaCO_3$ powder (diameter ~5 μm; Sakai Chemical Industry Co., Ltd, Osaka, Japan) and a methylcellulose-based binder (Matsumoto Yushi-Seiyaku Co., Ltd, Osaka, Japan) was extruded using an extruder (V-30 (II), Universe, Saga, Japan) through dies with a slit thickness of 200 μm and pitch of 500, 700, or 900 μm. HC green bodies with struts of ~200 μm in thickness and channels of ~300-, ~700-, or ~900 μm aperture size were obtained. The HC green bodies were heated at 600 °C for 24 h to remove the binder, resulting in the formation of $CaCO_3$ HC blocks. The $CaCO_3$ HC blocks were then immersed in 1 mol L^{-1} Na_2HPO_4 solution at 80 °C for 7 days. As a result, CAp HC scaffolds were formed *via* dissolution–precipitation reaction. Finally, the CAp HC scaffolds were precisely shaped into cylinders (diameter = 6 mm, height = 4 mm) using computer-aided design and computer-aided manufacturing (monoFab SPM-20; Roland DG, Shizuoka, Japan).

Characterization of HC Scaffolds

The crystal phases of the HC scaffolds were analyzed by X-ray diffraction (XRD; D8 Advance, Bruker AXS GmbH, Karlsruhe, Germany). Commercially obtained CAp granules (Cytrans, GC, Tokyo, Japan) were used as the reference. The chemical characteristics of the HC scaffolds were determined by Fourier transform infrared (FT-IR) spectroscopy (FT/IR-6200, JASCO, Inc., Tokyo, Japan). The microstructures of the HC scaffolds were analyzed by scanning electron microscopy (SEM; S3400N, Hitachi High-Technologies Corporation, Tokyo, Japan) and μ-CT imaging (SkyScan, Bruker Corporation, MA, USA). The carbonate content in the HC scaffolds was measured using elemental CHN (carbon–hydrogen–nitrogen) analysis (MT-6, Yanako Analytical Instruments, Kyoto, Japan). Eight samples per group were used to determine the average carbonate content. The total porosity of the HC scaffolds was calculated from the bulk density of the scaffolds and the theoretical density of HAp (3.16 g cm^{-3}), because the theoretical density of CAp is unknown. Eight samples per group were used to determine the average porosity. The compressive strength of the HC scaffolds was measured using a universal testing machine (Autograph AGS-J, Shimadzu Corporation, Kyoto, Japan). The samples were compressed with the load cell oriented parallel to their channels. Eight samples per group were used to determine the average compressive strength.

Surgical procedure

The animal experiments conducted in this study were approved by the Animal Care and Use Committee of Kyushu University (No. A30-338-1; issued Jun 13, 2019). Eighteen week-old male Japanese white rabbits (Japan SLC, Inc., Shizuoka, Japan) weighing 3.0–3.5 kg were used in the experiments. These rabbits were housed in the Center of Biomedical Research, Research Center for Human Disease Modeling, Graduate School of Medical Sciences, Kyushu University. Eighteen rabbits were used (n = 6). They were maintained on a standard diet with an adequate amount of water. Briefly, the rabbits were anesthetized with an intraperitoneal injection of a mixture of ketamine (30 mg kg^{-1}) and xylazine (5.0 mg kg^{-1}). The heads of the rabbits were shaved to remove the fur, and the skin was disinfected with 10% w/v povidone–iodine (Meiji Seika Pharma Co., Ltd, Tokyo, Japan). The calvarium was exposed through a skin incision ~2 cm in length over the linea media. The periosteum was incised in the same place and separated from the bone. Two HC scaffolds were implanted randomly in each animal on both sides of the sagittal suture without crossing it. The top surfaces of the HC scaffolds were covered with fasciae, and the fasciae were sutured. Finally, the wound was closed. The rabbits were allowed unrestrained movement in their cages after they recovered from the anesthesia.

Radiographic and histomorphometric analyses

The rabbits were euthanized in batches at 4 and 12 weeks after implantation of the HC scaffolds. The calvarium was harvested (n = 6 per group) to perform μ-CT imaging and histomorphometric analyses (to evaluate the resorption and bone formation abilities of the implanted HC scaffolds). Volumetric measurements of all specimens were performed by μ-CT (SkyScan) at a resolution of 18 μm. The percent volume of new bone within the HC scaffold and remaining scaffold was measured using software (CT Analyzer, Bruker). Following the radiographic analysis, the specimens were dehydrated using a graded series of alcohol solutions and embedded in polymethyl methacrylate histological resin (Technovit 9100; Heraeus Kulzer, Wehrheim, Germany). All specimens were cut into longitudinal sections throughout the cylindrical HC scaffold and HE-staining was performed. The histomorphometric analysis of HE-stained tissue sections was performed using a biological fluorescence microscope (BZ-X; Keyence Corporation, Osaka, Japan) with digital analysis software (BZ-X; Keyence Corporation). The height of new bone and the percent areas of the remaining materials and new bones in each scaffold channel were analyzed. For these analyses, 240 channels in HC230, 133 channels in HC460, and 90 channels in HC630 were used for each implantation period.

Statistical analysis

All data are presented as mean ± standard deviation. Results with $P < 0.05$ were considered statistically significant. Comparisons between groups were performed using the Tukey–Kramer test.

Conclusions

The channel aperture size of HC scaffolds exerted a significant influence on bone ingrowth and soft tissue invasion. The amount of new bone increased and the amount of soft tissues decreased with decreasing channel aperture size. The HC scaffolds with 230 μm-aperture channels possessed a higher ability for vertical bone augmentation than the various combinations of scaffolds and supplements that promote bone formation or act as barriers for soft tissue invasion. These findings indicate that the

multiscale-architectural control of HC scaffolds may help realize barrier membrane-free GBR.

Author contributions

K. Hayashi: Supervision; fabrication and characterization of materials; conduction, analysis, and interpretation of data in animal experiments; writing the initial draft; funding acquisition. M. Shimabukuro, R. Kishida, and A. Tsuchiya: conduction of animal experiments. K. Ishikawa: review and editing; funding acquisition. All authors have approved the final version of the manuscript.

Conflicts of interest

There are no conflicts to declare.

Acknowledgements

This study was supported in part by the Japan Agency for Medical Research and Development (grant numbers JP21he0422005j for Koichiro Hayashi and JP21im0502004h for Kunio Ishikawa), and the Japan Society for the Promotion of Science (grant number JP19K22970 for Koichiro Hayashi).

Notes and references

1 S. R. Kandavalli, Q. Wang, M. Ebrahimi, C. Gode, F. Djavanroodi, S. Attarilar and S. Liu, *Front. Mater.*, 2021, **8**, 646383.
2 S. Jayachandran, K. Hill and A. D. Walmsley, *Clin. Oral Implants Res.*, 2021, **32**, 659–671.
3 A. Rachmiel, D. Shilo, D. Aizenbud and O. Emodi, *J. Oral Maxillofac. Surg.*, 2017, **75**, 1164.
4 L. Cordaro and H. Terheyden, *Ridge Augmentation Procedures in Implant Patients: A Staged Approach*, ITI Treatment Guide, Quintessence Pub. Co., 2014.
5 C. Myeroff, M. Archdeacon and J. Bone, *J. Bone Jt. Surg., Am. Vol.*, 2011, **93**, 2227.
6 J. Waasdorp and M. A. Reynolds, *J. Oral Maxillofac. Surg.*, 2010, **25**, 525.
7 M. Chiapasco, M. Zaniboni and L. Rimondini, *Clin. Oral. Implants Res.*, 2007, **18**, 432.
8 P. Felice, G. Pellegrino, L. Checchi, R. Pistilli and M. Esposito, *Clin. Oral. Implants Res.*, 2010, **21**, 1394.
9 I. R. Zerbo, G. L. de Lange, M. Joldersma, A. L. Bronckers and E. H. Burger, *Clin. Oral. Implants Res.*, 2003, **14**, 759.
10 V. Venugopalan, A. R. Vamsi, S. Shenoy, K. Ashok and B. Thomas, *J. Clin. Diagn. Res.*, 2021, **15**, ZE01.
11 P. Aprile, D. Letourneur and T. Simon-Yarza, *Adv. Healthcare Mater.*, 2020, **9**, 2000707.
12 I. Elgali, O. Omar, C. Dahlin and P. Thomsen, *Eur. J. Oral Sci.*, 2017, **125**, 315.
13 C. S. Kim, S. H. Choi, J. K. Chai, K. S. Cho, I. S. Moon, U. M. Wikesjö and C. K. Kim, *J. Periodontol.*, 2004, **75**, 229.
14 I. A. Urban, E. Montero, A. Monje and I. Sanz-Sánchez, *J. Clin. Periodontol.*, 2019, **46**, 319.
15 B. Elnayef, A. Monje, J. Gargallo-Albiol, P. Galindo-Moreno, H. L. Wang and F. Hernández-Alfaro, *J. Oral Maxillofac. Surg.*, 2017, **32**, 291.
16 M. Esposito, M. G. Grusovin, P. Coulthard and H. V. Worthington, *J. Oral Maxillofac. Surg.*, 2006, **21**, 696.
17 Y. D. Rakhmatia, Y. Ayukawa, A. Furuhashi and K. Koyano, *J. Prosthodontics*, 2013, **57**, 3.
18 J. Garcia, A. Dodge, P. Luepke, H. L. Wang, Y. Kapila and G. H. Lin, *Clin. Oral. Implants Res.*, 2018, **29**, 328.
19 G. Lim, G. H. Lin, A. Monje, H. L. Chan and H. L. Wang, *J. Oral Maxillofac. Surg.*, 2018, **33**, 41.
20 J. R. H. Tay, X. J. Lu, W. M. C. Lai and J. H. Fu, *Int. J. Implant Dent.*, 2020, **6**, 76.
21 J. Jiménez Garcia, S. Berghezan, J. M. M. Caramês, M. M. Dard and D. N. S. Marques., *J. Prosthodontics*, 2017, **52**, 955.
22 P. Gentile, V. Chiono, C. Tonda-Turo, A. M. Ferreira and G. Ciardelli, *Biotechnol. J.*, 2011, **6**, 1187.
23 J. Liu and D. G. Kerns, *Open Dent. J.*, 2014, **16**, 56.
24 M. Toledano, S. Asady, M. Toledano-Osorio, F. García-Godoy, M. A. Serrera-Figallo, J. A. Benítez-García and R. Osorio, *Polymers*, 2020, **12**, 1290.
25 P. Abrahamsson, D. Å. Wälivaara, J. Anderud and R. Jimbo, *Clin. Exp. Dent. Res.*, 2017, **3**, 100.
26 J. S. Lee, J. S. Lee, M. H. Kang, U. W. Jung, S. H. Choi and K. S. Cho, *J. Biomed. Mater. Res., Part B*, 2018, **106**, 2700.
27 C. I. Polo, W. R. Sendyk, L. Correa, D. Sendyk, M. C. Z. Deboni and M. D. G. Naclério-Homem, *J. Periodontol.*, 2020, **91**, 1295.
28 J. P. Carrel, A. Wiskott, M. Moussa, P. Rieder, S. Scherrer and S. Durual, *Clin. Oral. Implants Res.*, 2016, **27**, 55.
29 W. Liu, B. Du, S. Tan, Q. Wang, Y. Li and L. Zhou, *Int. J. Nanomed.*, 2020, **10**, 10059.
30 H. Namli, Ö. Erdogan, G. Gönlüşen, O. E. Kahraman, H. M. Aydin, S. Karabag and U. Tatli, *Implant Dent.*, 2016, **25**, 54.
31 H. Zigdon-Giladi, D. Lewinson, T. Bick and E. E. Machtei, *J. Clin. Periodontol.*, 2013, **40**, 196.
32 F. Pieri, E. Lucarelli, G. Corinaldesi, N. N. Aldini, M. Fini, A. Parrilli, B. Dozza, D. Donati and C. Marchetti, *Biomaterials*, 2010, **31**, 3527.
33 H. Zigdon-Giladi, T. Bick, D. Lewinson and E. E. Machtei, *Clin. Implant Dent. Relat. Res.*, 2015, **17**, 353.
34 H. Zigdon-Giladi, T. Bick, E. F. Morgan, D. Lewinson and E. E. Machtei, *Clin. Implant Dent. Relat. Res.*, 2015, **17**, 83.
35 Y. Choi, J. H. Yun, C. S. Kim, S. H. Choi, J. K. Chai and U. W. Jung, *Clin. Oral. Implants Res.*, 2012, **23**, 682.
36 A. W. James, G. LaChaud, J. Shen, G. Asatrian, V. Nguyen, X. Zhang, K. Ting and C. Soo, *Tissue Eng., Part B*, 2016, **22**, 284.
37 J. Shen, A. W. James, J. N. Zara, G. Asatrian, K. Khadarian, J. B. Zhang, S. Ho, H. J. Kim, K. Ting and C. Soo, *Tissue Eng., Part A*, 2013, **19**, 2390.
38 K. Hayashi, N. Kato, M. Kato and K. Ishikawa, *Mater. Des.*, 2021, **204**, 109686.

Open Access Article. Published on 28 September 2021. Downloaded on 10/6/2024 4:17:07 PM. This article is licensed under a Creative Commons Attribution 3.0 Unported Licence.

© 2021 The Author(s). Published by the Royal Society of Chemistry

Open Access Article. Published on 28 September 2021. Downloaded on 10/6/2024 4:17:07 PM.
This article is licensed under a Creative Commons Attribution 3.0 Unported Licence.

39 Y. Xie, S. Li, T. Zhang, C. Wang and X. Cai, *Int. J. Oral Sci.*, 2020, **12**, 37.
40 K. Hayashi, M. L. Munar and K. Ishikawa, *Mater. Sci. Eng., C*, 2020, **111**, 110848.
41 K. Hayashi and K. Ishikawa, *ACS Appl. Bio Mater.*, 2021, **4**, 721.
42 K. Hayashi, R. Kishida, A. Tsuchiya and K. Ishikawa, *Adv. Biosyst.*, 2019, **3**, 1900140.
43 K. Hayashi and K. Ishikawa, *J. Mater. Chem. B*, 2020, **8**, 8536.
44 K. Hayashi, R. Kishida, A. Tsuchiya and K. Ishikawa, *Mater. Today Bio*, 2019, **4**, 100031.
45 K. Hayashi, R. Kishida, A. Tsuchiya and K. Ishikawa, *ACS Appl. Bio Mater.*, 2020, **3**, 1787.
46 T. Theophile, *Infrared Spectroscopy - Materials Science, Engineering and Technology*, IntechOpen, London, 2012, ch. 6.
47 H. Madupalli, B. Pavan and M. M. J. Tecklenburg, *J. Solid State Chem.*, 2017, **255**, 27.
48 E. D. Pellegrino and R. M. Biltz, *Nature*, 1968, **219**, 1261.
49 H. Guo, D. Xia, Y. Zheng, Y. Zhu, Y. Liu and Y. Zhou, *Acta Biomater.*, 2020, **106**, 396.
50 J. S. Lee, J. S. Lee, M. H. Kang, U. W. Jung, S. H. Choi and K. S. Cho, *J. Biomed. Mater. Res., Part B*, 2018, **106**, 2700.
51 D. Feldman and D. Ferguson, *J. Biomed. Imaging Bioeng.*, 2017, **1**, 35.
52 C. N. Brown and J. G. Finch, *Ann. R. Coll. Surg. Engl.*, 2010, **92**, 272.
53 D. S. Feldman, S. M. Hultman, R. S. Colaizzo and A. F. von Recum, *Biomaterials*, 1983, **4**, 105.
54 D. H. Kim, J. K. Cha, Y. W. Song, K. M. Woo and U. W. Jung, *J. Biomed. Mater. Res., Part B*, 2020, **108**, 1343.
55 Z. Sheikh, G. Chen, M. Thévenin, R. N. Young, M. D. Grynpas and M. Glogauer, *J. Oral Maxillofac. Surg.*, 2019, **34**, e51.
56 W. Liu, B. Du, S. Tan, Q. Wang, Y. Li and L. Zhou, *Int. J. Nanomed.*, 2020, **15**, 10059.
57 C. I. Polo, W. R. Sendyk, L. Correa, D. Sendyk, M. C. Z. Deboni and M. D. G. Naclério-Homem, *J. Periodontol.*, 2020, **91**, 1295.
58 J. P. Carrel, A. Wiskott, M. Moussa, P. Rieder, S. Scherrer and S. Durual, *Clin. Oral. Implants Res.*, 2016, **27**, 55.

© 2021 The Author(s). Published by the Royal Society of Chemistry